Simulation of Noise-Driven Wave Dynamics on a Falling Film

Hsueh-Chia Chang, Evgeny A. Demekhin, and Evgeny Kalaidin
Dept. of Chemical Engineering, University of Notre Dame, Notre Dame, IN 46556

A numerical model developed simulates inlet noise-driven wave dynamics on a falling film at relatively high Reynolds numbers. Two parameters, a normalized Reynolds number and a noise index, are sufficient to specify the wave statistics on most channels. Observed phenomena, like wave inception, downstream wave texture coarsening, initial deceleration and subsequent acceleration of wave speeds, are quantitatively reproduced and explained. Statistical analysis from our simulations suggests that beyond a critical Reynolds number this complex noise-driven spatio-temporal dynamics can be modeled by a deterministic interaction theory based on stable solitary waves that resemble one-hump pulses and a statistical theory with a random-phase description of noise. The "chaotic" wave dynamics at higher Reynolds number is hence due to both noise amplification/filtering and intrinsic dynamics.

Introduction

Interfacial heat and mass transport across thin films occurs in many industrial processes like sulfonation falling-film reactors, gas absorption towers, vertical condensers, evaporator tubes for desalination or in crystallizers, and so on. The transport rate in many of these processes is enhanced by physical obstacles which break up and reform the film after short distances. However, waves that appear on the interface are also known to enhance the interfacial transport process significantly (Frisk and Davis, 1972; Dukler, 1976; Henstock and Hanratty, 1979; Wasden and Dukler, 1989; Alekseenko et al., 1985). In a new design for desalination evaporator tubes, Li and Ho (1987) have found that specific waves excited by a whip rod can achieve enhancement factors of 2 to 3. However, it is generally agreed that transport enhancement by waves is most pronounced in absorption of dilute gases at high Peclet number since the transport there is across a concentration boundary layer at the interface which can be easily reformed by waves. Waves are also present on liquid films of many coating processes (Malamataris and Papanastasiou, 1991). These waves are obviously undesirable and considerable effort has been expended to understand how disturbances propagate and grow on thin films to better propose means of damping them (Kheshgi and Scriven, 1987).

While interfacial waves in an industrial process can be triggered by various forms of disturbances like gas turbulence and physical obstacles, the idealized problem of a freely falling film with inlet noise has become a classical hydrodynamic problem of fundamental interest since Kapitza (1948) first generated very regular wave patterns by pulsing the inlet flow rate. It was conjectured, as in many fields of engineering science, that wave dynamics and its effect on heat/mass transfer for this idealized problem should be understood first before more complex and practical systems can be tackled. Moreover, inlet noise-driven wave evolution on a falling film is actually a good model for many coating processes and understanding the wave dynamics of this idealized problem will help us reduce or control wave disturbances during coating. For this reason, noise-driven waves on a freely falling film have been scrutinized extensively in numerous experiments (Kapitza, 1948; Stainthorp and Allen, 1965; Krantz and Goren, 1971; Portalski and Clegg, 1972; Pierson and Whitaker, 1977; Alekseenko et al., 1985; Liu et al., 1993) and theoretical analyses (see reviews by Lin, 1983; Chang, 1994). However, wave evolution even for this idealized system remains extremely complex. In fact, it has become a prototype open-flow hydrodynamic instability which exhibits spatio-temporal chaos. Due to its complexity, our understanding of the underlying wave dynamics, particularly how it enhances heat/mass transfer, remains limited. With the development

Permanent address of E. A. Demekhin and E. Kalaidin: Dept. of Applied Mathematics, Kuban State Technological University, Krasnodar 350072, Russia.

of nonlinear theories and more sophisticated numerical tools, advances have been made. However, such theories are mostly applicable to highly idealized dynamics, such as periodically entrained waves, and do not shed much light on the complex spatio-temporal wave dynamics observed on a real film whose wave dynamics is noise driven. As we shall detail in this article, this dynamics is extremely irregular and only a statistical description is appropriate. However, the statistics are quite well-defined due to the unique structure of the pertinent waves, such that a comprehensive model is possible even for the complex dynamics.

The earliest theories on the subject are linear Orr-Sommerfeld type analyses (Benjamin, 1957; Yih, 1963) that determine the critical conditions when waves first become visible and the speeds and wavelengths of the Fourier wave modes that are most amplified at onset. It also identifies inertia as the cause of the instability. Another intriguing result of this classical analysis is that the waves at inception travel at twice the interfacial velocity of a flat film or three times the cross-film average velocity $< u >$ (Kapitza, 1948; Levich, 1962). This is a generic result that is independent of the liquid used. If the disturbances at the inlet, which is the main source of noise under realistic conditions, are broadbanded with many Fourier modes of small amplitude, the linear theory offers a good description of how most of the disturbances are filtered such that an almost periodic wave, corresponding to the fastest-growing mode, is observed at inception. If the noise amplitude is large or its Fourier content is narrow, this linear filtering mechanism does not fully manifest itself and if any monochromatic wave is selected, it may not be the fastest-growing one predicted by the linear theory. Moreover, as we shall see subsequently, the residual noise beyond inception still plays an important role in downstream wave dynamics.

The classical linear theory has recently been reanalyzed in various limits (Joo and Davis, 1992; Cheng and Chang, 1995) to show that wave inception on a falling film is a convective instability—a localized disturbance grows in a moving frame and not in a stationary frame. This implies that disturbances at the inlet are convected into the channel where they amplify and trigger secondary transitions. The linear theory is hence only applicable in the inception region near the inlet where the wave amplitude is small. This inception region is only 2 to 10 cm in length for a vertical film and slightly longer for inclined ones at realistic flow rates. Beyond this region, experimental data show significant deviation from the linear theory. Other than the fact that a nonlinear theory is imperative, the convective nature of the instability also suggests that the wave dynamics is extremely noise-sensitive. Periodic forcing at the inlet, for example, entrains periodic waves downstream while random forcing generates an entirely different kind of wave dynamics. Recent work on convectively unstable systems (see review by Huerre and Monkewitz, 1990) suggests that much of the dynamics in such systems are triggered by noise and its intrinsic nonlinear dynamics is often dominated or corrupted by the noise statistics. It is commonly believed that wave evolution on a falling film possess all the generic features of a convectively unstable system and understanding its dynamics will allow us to comprehend other chaotic dynamics in open-flow systems, including many turbulent flows. The practical advantage offered by falling-film dynamics over other classical open-flow instabilities, like channel and boundary layer flows, for this purpose is that its instability occurs at very low flow rates. For a vertical film, onset is at a vanishingly small Reynolds number. This allows simpler experimental and theoretical scrutiny. Yet, wave dynamics on a falling film exhibit a wide spectrum of wave transitions just as rich as the other flows, including the final transition to "interfacial turbulence."

Nonlinear theories for falling-film waves historically follow two approaches. One is a weakly nonlinear analysis that derives Stuart-Landau type amplitude equation for either the fastest-growing Fourier mode or a nearly neutral mode (Benney, 1966; Lin, 1969). It reveals that the linear growth beyond inception will be saturated by nonlinear interaction and the waves will be decelerated by the same mechanism. Other than an estimate of the saturated wave amplitude and speed, this theory offers little insight beyond the saturation stage. The saturated waves survive only for about 10 cm beyond the inception region. They then trigger a series of further transitions whose sequence and duration seem to be sensitive to noise at the inlet. Most of the triggered waves have large amplitudes such that the classical weakly nonlinear analysis does not apply. Under noise-driven inlet forcing, they are also too irregularly spaced to defy a periodic description.

To simplify the problem, periodic inlet forcing has been used in experiments to entrain periodically spaced waves (Kapitza, 1948; Alekseenko et al., 1985). With a sufficiently large forcing amplitude, the inception region can be eliminated entirely such that large-amplitude periodic waves, whose wavelengths are stipulated by the forcing frequency and not selected by an inception region, are generated immediately downstream. These artificially excited waves are easier to construct, and they have spurred a generation of theoretical investigation on periodic waves. In these studies, to avoid tackling the full Navier–Stokes equation, lubrication-type long-wave approximation has been used to derive equations that are sometimes called Benney's equation (Joo et al., 1991). The earlier equations consider only weak inertia, the key destabilizing mechanism, and hence are limited to low Reynolds number films. Shkadov (1967) first derived a set of ad hoc model equations known as the averaged equations that allow scrutiny of flow conditions at high Reynolds number. However, recent numerical studies of periodic waves have revealed that, while the averaged equations offer qualitatively correct periodic wave structures, their quantitative accuracy begins to deteriorate beyond $R = 10$ for water (Chang, 1994), where $R = \langle q \rangle / \nu = \langle u \rangle h_0 / \nu$ is the flow rate based Reynolds number. In contrast, Benney's equation does not even reproduce qualitatively correct periodic waves beyond $R = 5$ (Salamon et al., 1994). We shall also show here that the wave dynamics at low inertia is quite different from high-inertia dynamics. As a result, such equations are limited to low-inertia films encountered mostly in evaporator and condenser tubes. They offer some qualitative insight but little quantitative accuracy for thicker films with $R > 10$. Analytical and numerical tools introduced by modern dynamical systems have permitted the construction of traveling wave solutions to the various model equations, including the Navier–Stokes equation. Earlier normal form and center manifold projection analyses reveal families of periodic, solitary, and shock traveling waves (Chang, 1987, 1989). Some of these were then

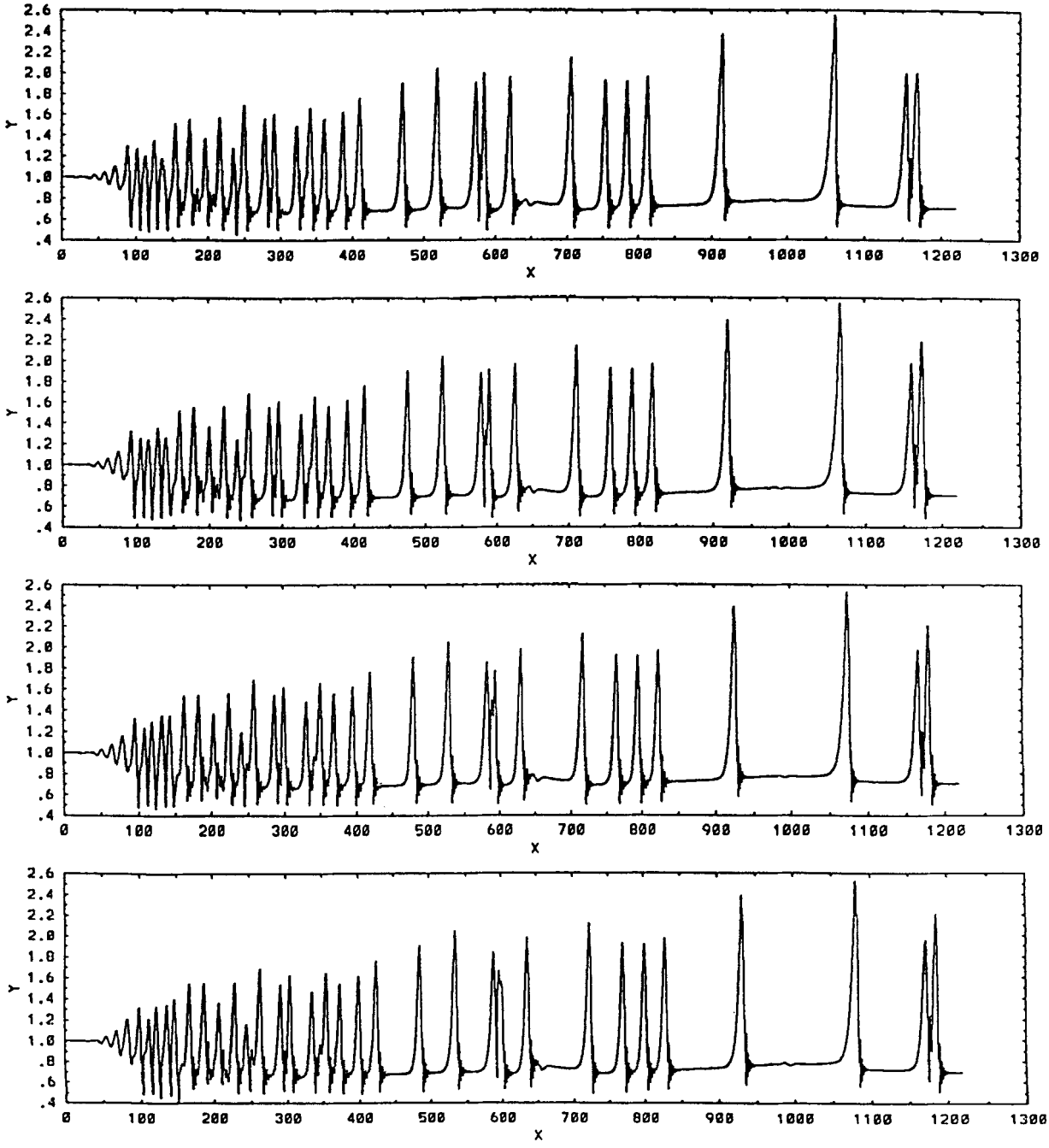

Figure 1. Wave profile at $t=211$, 212, 213, and 214 for $\delta=0.216$, $\omega_*=2\omega_0=2\times1.972$ and $F_0=1\times10^{-4}$.
All units are dimensionless.

numerically traced (Chang et al., 1993; Salamon et al., 1994). It was from the comparison of the periodic wave solution branches of the various models to those of the full Navier–Stokes equation by Salamon et al. that determined the limitation of the simplified model equations.

However, it should be reminded that periodic waves are artifacts of our problem formulation. With natural forcing, large-amplitude periodic traveling wave solutions are almost never observed unless they are entrained with periodic forcing (Chang et al., 1993). Chang et al. (1994) have shown that, for noise-driven wave dynamics, only the small-amplitude waves just beyond inception can be modeled as periodic traveling waves. Stability analysis carried out by Chang et al. (1993, 1994) determined the selected periodic traveling wave out of infinitely many others. Its wavelength is actually shorter than the fastest growing linear mode such that the nonlinear mechanism that saturates and decelerates the monochromatic wave also compresses it. Beyond inception, however, this periodic wave rapidly precipitates the formation of pulse-like solitary waves, as shown in Figure 1. With broad-banded forcing at the inlet, the spacing of these pulses is typically very irregular as they feel the residual effect of noise at the inlet beyond inception and only occasional patches resemble periodic trains of pulses. Until transverse variation

sets in, the wave dynamics downstream from inception is dominated by these pulses. They are hence the most important traveling waves while periodic waves are only important near the inception region. In tubes and columns, the transverse variation is actually suppressed (Cheng and Chang, 1992). Even if the transverse variations are pronounced, unless they actually pinch off the crests, the waves still resemble modulated pulses (Chang et al., 1994).

Solitary pulse traveling wave solutions have been constructed from the Kuramoto-Sivashinsky equation, Benney's equation (Tsvelodub, 1980; Pumir et al., 1983) and the averaged equations (Demekhin and Shkadov, 1985). However, the observed dynamics for the first two equations are quite distinct from those of the latter for thicker, higher inertia films. The solitary pulses are only stable when inertia exceeds a critical value (Chang et al., 1995b) beyond the region of validity of the KS and Benney equations. Chang et al. (1995a) have used the averaged equations to demonstrate that the downstream spatio-temporal dynamics for high-inertia films is dominated by mutual interaction between pulses and by the intermittent coalescence events that widen the pulse spacing downstream. The frequency of the latter events is found to be sensitive to the initial inlet noise. With the above discovery and the experiments by Liu and Gollub (1994) on solitary pulse interaction, it has become hopeful that there is some underlying structure to the chaotic wave dynamics at higher flow rates that allows a rational deterministic description. There is even hope that the noise sensitivity can be described quantitatively with a simple description. However, to achieve both, one must abandon the inaccurate averaged equation since even its periodic waves cannot be quantitatively compared to experimental data. Much of the interesting dynamics, driven by pulse interaction and coalescence, evolves over a length scale in excess of 1 m. Due to this excessive computation domain, extensive simulation with the Navier–Stokes equation with realistic inlet noise is still impossible although successful results for short channels (Khesghi and Scriven, 1987) and periodic domains (Ho and Patera, 1990; Salamon et al., 1994) have been reported.

Instead, we shall use the boundary layer (BL) equation

$$\frac{\partial u}{\partial t}+u\frac{\partial u}{\partial x}+v\frac{\partial u}{\partial y}=\frac{1}{5\delta}\left(h_{xxx}+\frac{1}{3}\frac{\partial^2 u}{\partial y^2}+1\right)-3\chi\frac{\partial h}{\partial x} \tag{1a}$$

$$v=-\int_0^y \frac{\partial u}{\partial x}\,dy \tag{1b}$$

$$\frac{\partial h}{\partial t}=-\frac{\partial}{\partial x}\int_0^h u\,dy \tag{1c}$$

$$y=h(x,t) \qquad \frac{\partial u}{\partial y}=0 \tag{1d}$$

$$y=0 \qquad u=0 \tag{1e}$$

The BL equation is obtained by omitting the second derivative $\partial^2/\partial x^2$ term in the momentum equation and invoking the longwave approximation $\partial/\partial y \gg \partial/\partial x$, which provides a much simpler and yet accurate substitution. The parameter $\chi=\cot\theta/R$ measures the inclination angle θ from the horizontal. We shall focus here on the case of a vertical film with $\theta=\pi/2$ and $\chi=0$. The lone parameter for the system is then the scaled Reynolds number measuring inertia

$$\delta=\frac{R^{11/9}(\sin\theta)^{1/9}}{5\gamma^{1/3}3^{7/9}} \tag{2}$$

where $\gamma=\sigma/\rho\nu^{4/3}g^{1/3}$ is the Kapitza number which is dependent only on the physical properties of the fluid. For example, $\gamma=2{,}850$ for water at 15°C. The Reynolds number $R=\langle u\rangle h_0/\nu$ is based on the average fluid velocity $\langle u\rangle$ and the Nusselt flat-film thickness h_0. The normal velocity has been scaled by $\langle u\rangle/\kappa$ while the tangential velocity by $\langle u\rangle$ where $\kappa^3=\sigma/(\rho g h_0^2\sin\theta)$. This large parameter κ measures the ratio between the tangential and normal length scales exploited in the longwave approximation. Similarly, the downstream tangential coordinate x has been scaled by $h_0\kappa$, the normal coordinate y by h_0 and time by $h_0\kappa/\langle u\rangle$. A major advantage offered by the BL simplification is that the original three parameters (Weber, Reynolds, and inclination angle) have been reduced to only δ and χ. For a vertical film, only one parameter is sufficient to specify the problem. The term BL equation is used because the same "longwave" approximation is made in classical momentum and concentration boundary layer theories. However, the boundary layers grow downstream in the latter problems while surface tension prevents our film from doing the same. Also, at small δ, the BL equation reduces to both the Benney and Kuramoto-Sivashinsky equations (Chang et al., 1993). It hence also captures low-inertia dynamics faithfully.

The omission of the $\partial^2/\partial x^2$ term also parabolizes the equation and greatly reduces the numerical effort. We refer the readers to an earlier publication (Chang et al., 1993) for a systematic derivation of this equation and an estimate of the resulting error. In general, the longwave approximation remains valid at low flow rates when the wave slope is small. Salamon et al. have shown in their construction of periodic wave solution branches from the full Navier–Stokes equations that, except for some details near the bifurcation points of the solution branches, the BL equation offers a quantitatively accurate description for $R<300$. With Eqs. 1 we shall demonstrate that realistic wave dynamics at high inertia is indeed driven by pulse interaction and coalescence. More importantly, the measurable and meaningful statistical characteristics of the wave dynamics are parameterized by only δ and another index representing the noise amplitude at the inlet. The BL equation is hence an accurate and simple model for extended channel wave dynamics. The representation of broadbanded noise by a single index also suggests that statistical theory describing the pulse interaction and coalescence that drive the downstream wave dynamics is within reach.

Numerical Formulation

Solution of Eqs. 1 in an extended domain requires boundary conditions at both ends of the channel. We have examined two kinds of distributors at the inlet: a closed-channel distributor of height H found in many coating processes (Khesghi and Scriven, 1987) corresponding to the boundary condition at $x=0$

$$u = \frac{6}{H}\left(\frac{y}{H} - \frac{y^2}{H^2}\right)[1 + F(t)] \tag{3a}$$

$$h = H \neq 1 \tag{3b}$$

and an open-channel distributor with a flat film

$$u = 3(y - y^2/2)[1 + F(t)] \tag{4a}$$

$$h = 1 \tag{4b}$$

Since the y-dependent disturbances damp much faster than the mean-flow in a flat film or a closed channel, we have neglected all y-dependent disturbances and lumped the forcing within the flow-rate fluctuation $F(t)$ which has a zero mean

$$\langle F \rangle = \lim_{T \to \infty} \frac{1}{T} \int_0^T F(t)dt = 0 \tag{5}$$

We are hence imposing a constant mean flow-rate boundary condition with zero-mean fluctuations. As such, condition 3a is also augmented by the following constraint that specifies H

$$\int_0^H \frac{6}{H}\left(\frac{y}{H} - \frac{y^2}{H^2}\right)dy = 1 \tag{6}$$

The boundary conditions at the exit at $x = L$ are more troublesome. As first formulated by Fasel et al. (1987) for other convectively unstable open flows, the best strategy here is to abandon any attempt to model reality but to formulate "soft" boundary conditions that minimize the generation of upstream propagating disturbances to enhance numerical stability. This is permitted since the convective nature of the instability stipulates a predominantly downstream evolution of disturbances. Due to the length of the domain, the region affected by upstream propagation of disturbances generated by the exit is only a small fraction of the entire channel. One may then minimize the creation of exit noise to prevent numerical error and reduce computational domain. Roberts (1992) has formulated a systematic derivation of such boundary conditions using invariant manifold theories. We shall, however, adopt only the main idea here which is to induce the film to decay to the flat-film solution at the exit and hence minimize the generation of noise. (This amounts to forcing the system to approach the stable manifold of the flat film in the language of the invariant manifold theory.) In a nonstationary problem where the linear problem can be Fourier transformed in time, the spatial eigenvalues that dictate how the film approaches the flat-film solution vary from one frequency mode to another. To select a unique exit condition, we choose the zero frequency mode and force the steady film to approach the flat-film solution at the exit. Linearizing Eq. 1 about $h^* = 1$ and $u^* = 3(y - y^2/2)$, one obtains for the linear steady problem

$$\varphi_{yyy} - 15\delta\sigma[u^*\varphi_y - u_y^*\varphi] = 3\sigma^3 \tag{7a}$$

$$y = 1 \qquad \varphi_{yy} = -3, \qquad \varphi = 3/2 \tag{7b}$$

$$y = 0 \qquad \varphi = \varphi_y = 0 \tag{7c}$$

where φ is the disturbed tangential velocity divided by σ, the spatial eigenvalue. The countable infinite number of spatial eigenvalues $\sigma_i(\delta)$ can be obtained with a routine solver, and we find the first two to be a complex conjugate pair with positive real parts. These two modes grow in the positive x direction and must hence be suppressed. The other eigenvalues have negative real parts and we choose the largest one $\sigma(\delta)$, which is always real, and stipulate

$$x = L \qquad \frac{\partial h}{\partial x} - \sigma(h - 1) = 0 \tag{8a}$$

$$\frac{\partial^2 h}{\partial x^2} - \sigma\frac{\partial h}{\partial x} = 0 \tag{8b}$$

such that the "unstable" complex pair is always suppressed. Note that when $\sigma = -\infty$, one obtains the usual Danckwerts exit boundary conditions $h = 1$ and $\partial h/\partial x = 0$ at the exit. However, Eq. 8 is a more precise since σ is typically finite.

We can describe the above approach in more physical terms. An exit boundary condition introduces a perturbation to traveling wave patterns. The disturbances triggered by the perturbed wave pattern can propagate upstream and corrupt the wave dynamics in the computational domain. They can also cause numerical instability. These undesirable effects occur because the true exit condition can never be simulated without expending considerable numerical effort to resolve the exit channel. The solution taken here is to force the time-averaged interface to a flat one at the exit. Since all disturbances triggered by a flat interface travel downstream, upstream disturbances propagation caused by the artificial condition is considerably minimized. It is not entirely removed since we are only dampening the zero-frequency mode. This concept of "soft" boundary conditions was used by Fasel et al. (1987) and Roberts (1992). The artificial flat film is seen at the exit end of the computational domain in Figure 1. Consequently, although the computational domain extends to $x = 1{,}300$ in Figure 1, wave profiles are presented only up to $x = 1{,}200$. All subsequent figures have been similarly truncated to remove the artificial flat film due to the "soft" exit boundary condition.

We shall use a domain transformation $\eta = y/h(x, t)$ to transform the film into a long rectangle between $x \epsilon (0, L)$ and $\eta \epsilon (0, 1)$. We then use a Petrov-Galerkin expansion in the η direction, using polynomial bases that resemble the velocity profile, and an implicit finite-difference discretization in time and x. Only the Petrov-Galerkin expansion will be detailed here. The finite-difference scheme is similar to that of Demekhin et al. (1987) for the construction of traveling solitary waves for the BL equation.

The bases $\{\psi_k(\eta)\}_{k=1}^N$ for $u(\eta, x, t)$ in the η direction are chosen to satisfy boundary conditions (Eqs. 1d and 1e), viz.

$$\psi_k(0) = 0 \qquad \frac{\partial \psi_k}{\partial \eta}(1) = 0 \tag{9}$$

The first basis is chosen to be the parabolic profile

$$\psi_1 = \eta - \eta^2/2 \tag{10}$$

and the rest are chosen as

$$\psi_k = \eta^k - \frac{k}{k+1}\eta^{k+1} \tag{11}$$

If the number of bases N is large, it is clear from Eq. 11 that the higher bases become almost linearly-dependent and a Gram-Schmidt procedure may be necessary to produce two biorthogonal bases. However, for $R < 300$, the film is very thin and the profile is almost parabolic such that N is never larger than 7. Convergence with respect to N was carefully verified in our numerical study. We can hence use bases (Eq. 11) directly.

Expanding u by $\{\psi_k\}$ in the following convenient manner

$$u(x,\eta,t) = \frac{1}{h(x,t)} \sum_{k=1}^{N} A_k(x,t)\psi_k(\eta) \tag{12}$$

the vertical velocity becomes simply

$$v(x,\eta,t) = -\sum_{k=1}^{N} \frac{\partial A_k}{\partial x}\bar{\psi}_k(\eta) + \eta u \frac{\partial h}{\partial x} \tag{13}$$

where

$$\bar{\psi}_k = \frac{1}{k+1}\left(\eta^{k+1} - \frac{k}{k+2}\eta^{k+2}\right)$$

Substituting Eq. 12 and Eq. 13 into Eq. 1 and taking inner-product over $\eta\epsilon(0,1)$ with the weighting functions $\{\phi_k\}_{k=1}^{N}$, where $\phi_k = \eta^{k-1}$ are convenient weighting functions often used in boundary layer theory one obtains

$$a_{km}\frac{\partial A_m}{\partial t} + b_{kml}\frac{\partial}{\partial x}\frac{A_m A_l}{h} + c_{kml}\frac{A_l}{h}\frac{\partial A_m}{\partial x} = \frac{1}{5\delta}\left[h\left(\frac{\partial^3 h}{\partial x^3} + 1\right)\delta_{k1} + d_{km}\frac{A_m}{3h^2}\right] \tag{14a}$$

$$\frac{\partial h}{\partial t} + a_{1m}\frac{\partial A_m}{\partial x} = 0 \tag{14b}$$

where

$$\delta_{k1} = \begin{matrix} 0 & k \neq 1 \\ 1 & k = 1 \end{matrix} \tag{15}$$

and the Einstein summation notation has been used. The tensors a, b, c and d are determined from the inner products $\int_0^1 \varphi_k \psi_m d\eta$, $\int_0^1 \varphi_k \psi_m \psi_l d\eta$ and $\int_0^1 \varphi_k \psi_m \bar{\psi}_l d\eta$. Because of the simplicity of the bases and weighting functions, they can actually be written explicitly without numerical integration. The next step is then to use a fourth-order finite-difference scheme in x for h in Eq. 14 due to the $\partial^3 h/\partial x^3$ term and a first-order scheme in x for A_m. A fully implicit scheme is then used where the time derivative $\partial h/\partial t$, for example, is approximated by $[h(t_{n+1}) - h(t_n)]/\Delta t$, but all other quantities are evaluated at t_{n+1}. A set of nonlinear algebraic equations must then be solved at every time step, and we use a Newton scheme which usually requires fewer than 4 iterations per time step. Solution of the linear equation by LU decomposition during each iteration is found to be unstable. Instead, we use a triangulation formulation by transforming the matrix A to a triangular one T with the transformation

$$T = PA \tag{16}$$

where P is a product of orthogonal matrices. The linear equation is then solved by backward recurrence during the Newton iteration scheme.

The final information needed is the specification of the zero-mean fluctuation $F(t)$ for the flow rate. We have chosen the following random-phase characterization of noise. Fourier transforming $F(t)$ in time and decomposing the Fourier coefficient into modulus and phase components

$$F(t) = \int_0^\infty \hat{F}(\omega)e^{-i\omega t}d\omega = \int_0^\infty |\hat{F}(\omega)|\, e^{i\theta(\omega) - i\omega t}d\omega \tag{16}$$

where $\theta(\omega)$ is the phase of the complex amplitude $\hat{F}(\omega)$. We approximate Eq. 16 with M frequency units of width $\Delta\omega = \omega_*/M$ where ω_* is some high frequency cutoff. Hence

$$F(t) \sim \sum_{k=1}^{M} |\hat{F}(\omega)|\, e^{-ik\Delta\omega t + i\theta(\omega_k)}\Delta\omega \tag{17}$$

where $\omega_k = k\Delta\omega$, and we have omitted the amplitudes of all modes with frequencies larger than ω_*. The phase $\theta_k = \theta(\omega_k)$ is taken from a random number generator from the range $\theta_k \epsilon [0, 2\pi]$ and $|\hat{F}(\omega)|$ can be arbitrarily specified. We have found that most experimental data can be simulated with a cutoff frequency $\omega_* = 2\omega_0$, where ω_0 is the wave-frequency of the neutral mode calculated by Chang et al. (1993). It is approximately $\sqrt{18\delta}$ in dimensionless form which is of the order of 10 Hz for water under most conditions. We also impose a piecewise constant forcing spectrum of

$$\begin{aligned} |\hat{F}(\omega)| &= F_0 \quad \omega < \omega_* \\ &= 0 \quad \omega > \omega_* \end{aligned} \tag{18}$$

With $M = 1{,}000$ such that the results are independent of M. Therefore, the noise is fully characterized by the single index F_0 in this representation if the default cutoff frequency $\omega_* = 2\omega_0$ is used. A program GALA has been prepared in a package form to allow easy usage with arbitrary assignment of ω_* and $|\hat{F}(\omega)|$. Each run of duration $t = M/2\omega_0 = 500/\omega$ and channel length $L = 2{,}000$, corresponding to roughly 2 m, requires about 400 to 500 h of CPU time on a Convex computer.

Numerical Experiment

A typical run with the open-channel distributor (Eq. 4) at $\delta = 0.216$, $\omega_* = 2\omega_0 = 2 \times 1.972$ and $F_0 = 1 \times 10^{-4}$ is shown in Figure 1. The snapshots in Figure 1 show an inception region of 50 units, corresponding to 5 cm for water at $R = 18.75$. (A good rule of thumb for the present conditions is that one dimensionless unit in the x-direction corresponds to

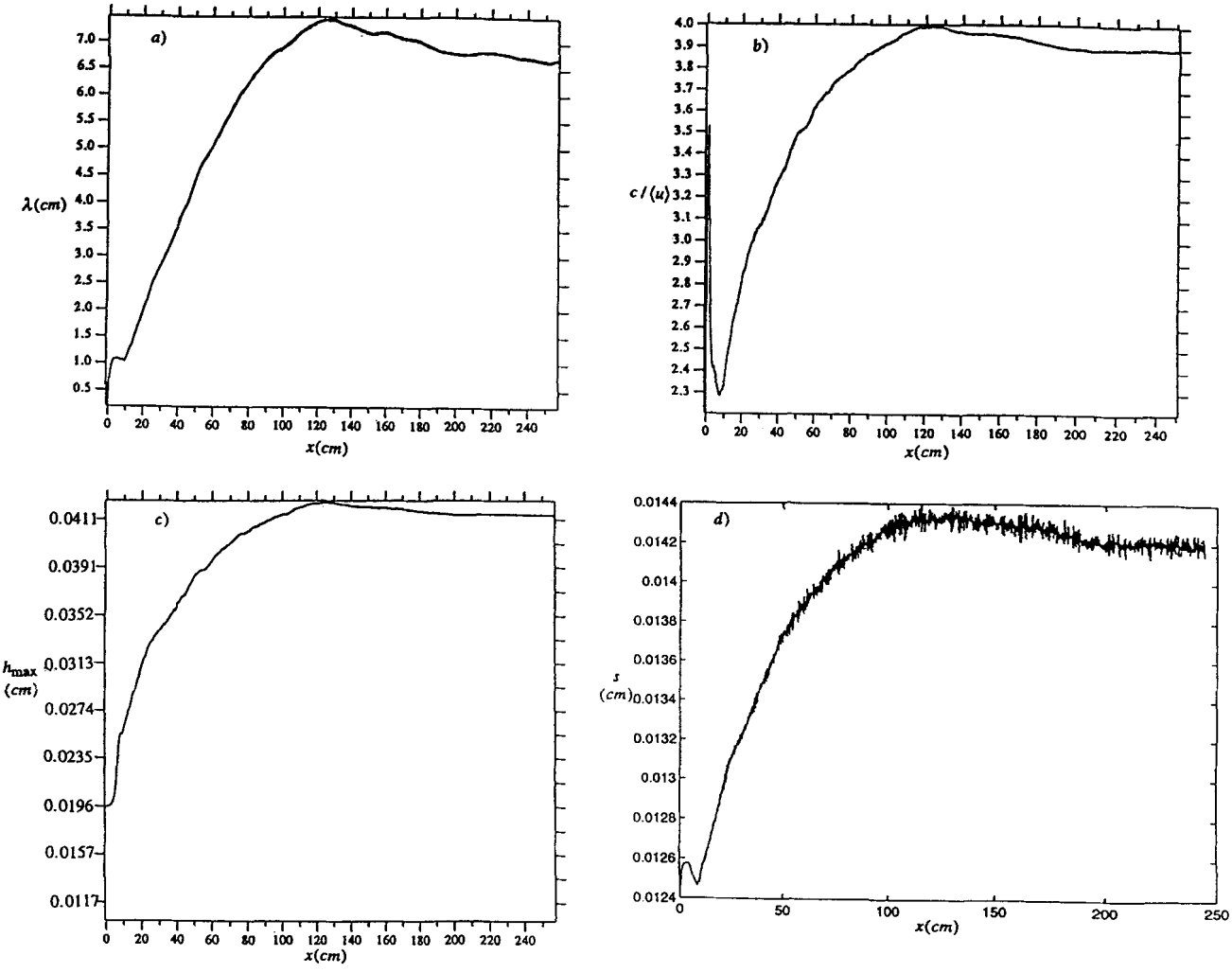

Figure 2. Time-averaged quantities of conditions in Figure 1 at various spatial locations for (a) spacing, (b) scaled speed, (c) film maximum and (d) film substrate thickness.

Dimensional quantities are shown.

0.1 cm.) The waves beyond inception quickly develop into pulse-like structures at 100 units and all subsequent pulses have qualitative similar shapes with a steep front preceded by small bow waves. The amplitude and spacing between pulses seem to grow slowly within the 1,300 unit domain (130 cm for water at $R = 18.75$). As demonstrated by Chang et al. (1995a), this gradual increase in the average spacing is caused by an irreversible coalescence of adjacent pulses to form a single pulse. Two coalescence events are seen at $x \sim 600$ and 1,200. Figure 2 depicts the time-averaged separation, pulse speed, pulse amplitude and substrate thickness as functions of downstream distance. The coarsening evolution of the wave texture is clearly evident. The time-average speed shows a unique behavior that was observed much earlier by Stainthorp and Allen (1965) whose work remains the most accurate recording of how wave velocity and wave profile evolve downstream. It drops precipitously from the onset wave speed of about three times the average film velocity $\langle u \rangle$ in the inception region to 2.2 $\langle u \rangle$ at the end of the inception region at $x = 50$. This drop corresponds to the weakly nonlinear deceleration mechanism first predicted by earlier nonlinear theories (Kapitza, 1948; Shkadov, 1967; Lin, 1969). A slight decrease in the wavelength λ is also evident here at about 10 cm. This is consistent with our result (Chang et al., 1993, 1994) that the finite-amplitude monochromatic wave selected after the inception region is slower and shorter than its small-amplitude precursor within the inception region.

However, these monochromatic waves quickly lose their periodic structure soon after they exit the inception region and trigger the formation of pulses. We find from our simulations that the only exceptions to this scenario of secondary pulse formation occur for the low flow-range of δ less than about 0.03, corresponding to R less than 2.0 for water. Under these extreme conditions, the inception region is extremely long and the wave structure of the saturated waves beyond it are of small-amplitude and irregular shape. They resemble localized saturated monochromatic waves. This near-critical exception to the generic scenario of pulse generation lies in the region where the Kuramoto-Sivashinsky (KS) equation or its generalization, the generalized KS equation, is a valid model (Chang, 1994). We have recently shown that the reason for this deviant behavior is that the pulse traveling

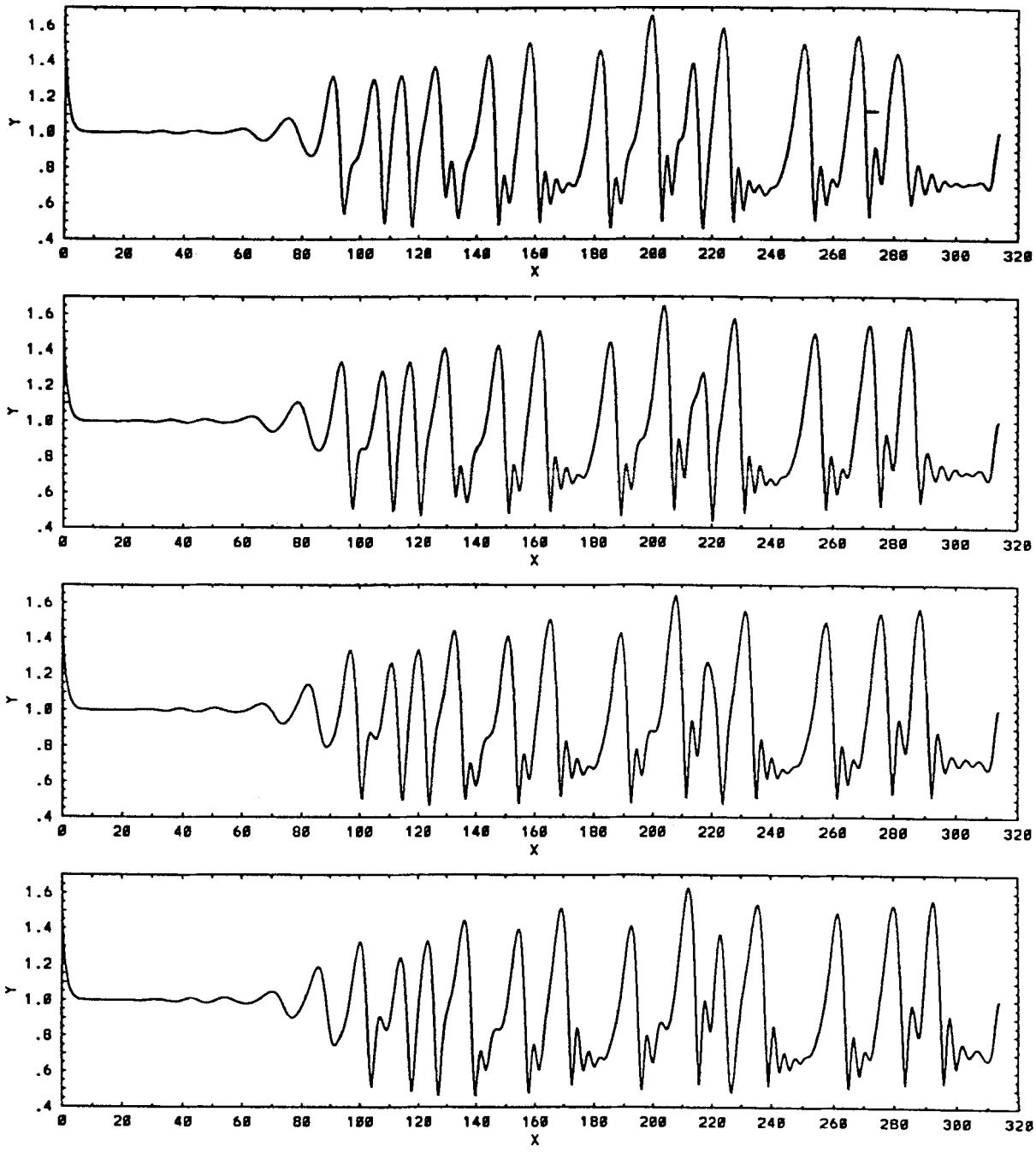

Figure 3. Closed distributor at $t = 98, 99, 100$ and 101 for $\delta = 0.216$, $\omega_* = 2\omega_0 = 2 \times 1.972$, $F_0 = 1 \times 10^{-4}$ and $H = 1.5$.

wave solution is "convectively" unstable, in a sense analogous to the classical convective stability theory for a flat film, below a critical δ (Chang et al., 1995b) and hence will never evolve from the inception region. Instead, one sees the highly irregular and small-amplitude KS chaos that has been of some interest recently. However, at higher flow rates when inertia is significant, the distinct large-amplitude pulses are stable. They appear beyond the inception region as seen in Figure 1 at higher values of δ and their dynamics is quite generic. The spacing between these pulses is still denoted λ, and it is observed to increase downstream in Figure 2. As the pulses spread out, their average speed also increases downstream. Both the coarsening and the acceleration seem to evolve in a roughly linear manner with respect to x. At $x \sim 800$ units (~ 80 cm), both the spacing and the speed have saturated at their equilibrium values. The average amplitude of the pulses also increases downstream until it also saturates at 800 units. The substrate thickness s on the other hand drops by 50% within the inception region since most of the liquid is drained into the pulses. As a result, a gradual upward drift of the average substrate thickness downstream, in parallel with the coarsening and acceleration, can be detected. The final saturation at 800 units seems to occur because the flat substrates between pulses has increased its width to such an extent that

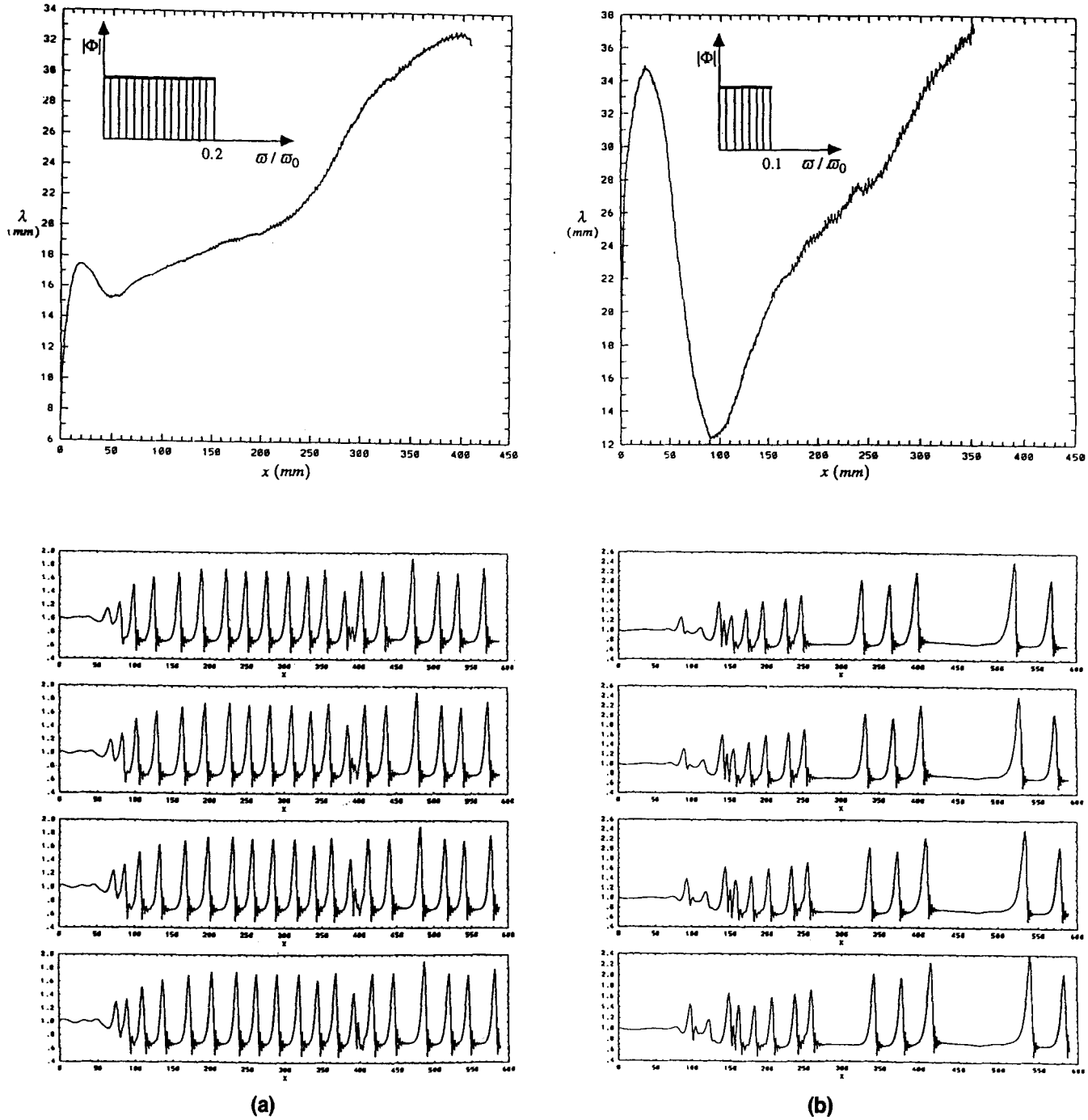

Figure 4. Time-averaged spacing of narrow-banded forcing with (a) $\omega_* = 0.2\,\omega_0$ and (b) $\omega_* = 0.1\omega_0$.

Conditions are the same as Figure 1 and 313, 314, 315 and 316 for (a) and t = 244, 245, 246 and 247 for (b).

new pulses begin to nucleate on them. When this balances the coalescence rate, the pulse density and hence, pulse speed and substrate thickness, reach statistically stationary values.

Before we explore the statistics of this evolution in more detail, we shall examine several other factors. In Figure 3, the closed channel distributor is used for the same conditions as in Figures 1 and 2 with $H = 1.5$. It is seen that the film height quickly drops from 1.5 of the channel height to 1.0 and since the closed channel flow is more stable, the inception region is lengthened somewhat compared to Figure 1. However, subsequent evolution is quite analogous to the open-channel distributor. We hence conclude that for small-amplitude forcing the distributor has little effect on the wave dynamics. We also experimented with narrow-banded forcing. As seen in Figure 4 for $\omega_* = 0.2\ \omega_0$ and $0.1\ \omega_0$, the wave dynamics is now quite different with more regularly spaced pulses due to the narrow-banded noise spectrum. For $\omega_* = 0.1\ \omega_0$, the spacing is so large that now pulses begin to nucleate between the pulses right after the inception region instead of evolving directly from the inlet disturbance. One

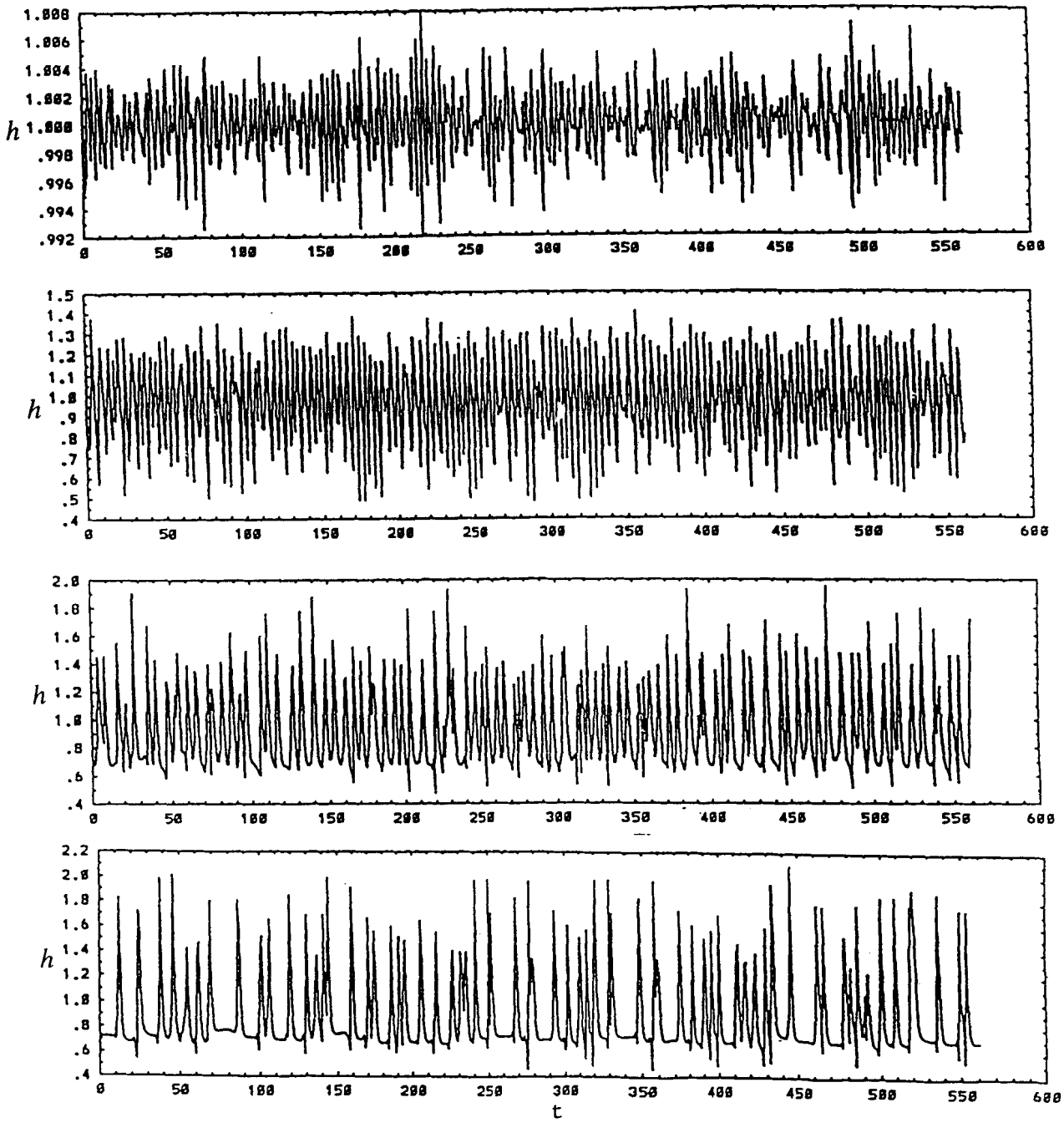

Figure 5. Wave tracing in time at x = (a) 30, (b) 100, (c) 250 and (d) 500 units for conditions of Figure 1.

nucleating pulse is seen at $x = 120$. Such regular wave dynamics is never observed in realistic noise-driven experiments although Liu and Gollub (1994) and Liu et al. (1993) have artificially introduced periodic forcing at the inlet to entrain periodically spaced pulses seen in Figure 4a. With $\omega_* \sim \omega_0$ or higher, the dynamics is again insensitive to ω_* and is only a function of δ and F_0.

In the case of broadbanded forcing in Figure 1, the linear filtering mechanism that selects a single monochromatic wave is very effective even though a large band of equal-amplitude disturbance is in play. This is evident in the wave tracing of Figure 5 at $x = 100$. Even though some envelope modulation is present, the waves are almost monochromatic. Compare this to the irregular tracing at $x = 30$ where the random noise is still felt and to the pulse-like shapes at $x = 500$. To make this selection process more precise, we evaluate the spatial eigenvalues $\alpha_k(\omega)$ at a given frequency. (See Cheng and Chang, 1995, for a derivation of spatial evolution theory for the averaged equations. There is an infinite number of such spatial eigenvalues from the linearized equation and the film thickness evolves as

$$h - 1 = \int_0^\infty \sum_{k=1}^{\infty} \phi_k(\omega) e^{i[\alpha_k(\omega)x - \omega t]} d\omega \qquad (19)$$

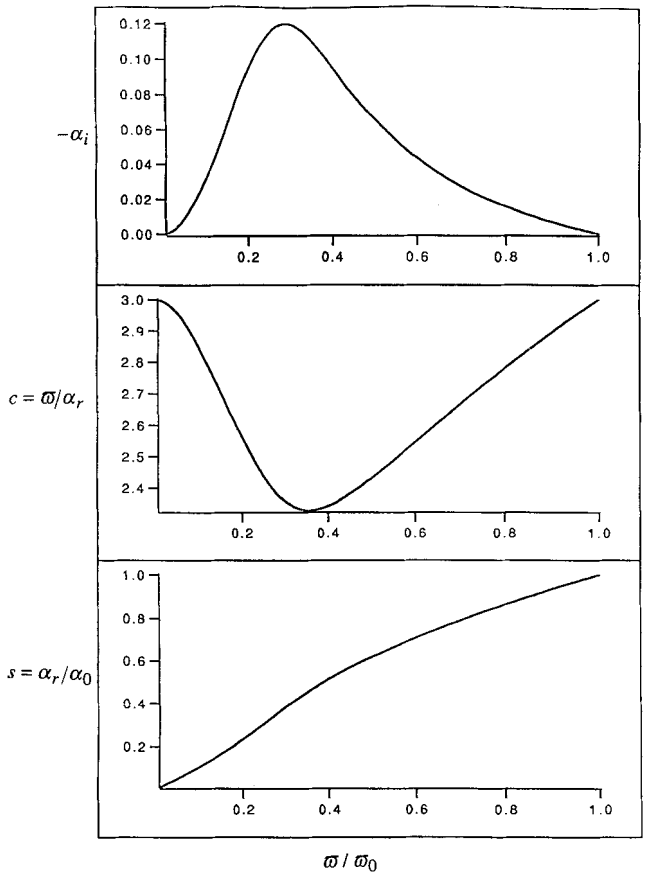

Figure 6. Linear spatial growth rate, wave speed, and wave number as a function of wave frequency for conditions of Figure 1.

and $\phi_k(\omega)$ is the unspecified Fourier coefficient. Of the infinite number of spatial eigenvalues, only one with growth rate α_1 is physically appropriate since it propagates downstream with a positive spatial growth rate: $-\alpha_1^i = -Im\{\alpha_1\} > 0$ and $\alpha_1^r = Re\{\alpha_1\} > 0$ for $\omega\epsilon(0, \omega_0)$. For $\delta = 0.216$, this mode exhibits a maximum in $-\alpha_1^i$ at $\omega_m \sim 0.290\ \omega_0$ where the growth rate is $-\alpha_{1m}^i = 0.120$, as shown in Figure 6. Omitting all modes except α_1 in Eq. 19, it is clear that the maximum and minimum of $h-1$ correspond to when the real part of $e^{i[\Theta-\omega t+\alpha_1^r x]}$ is equal to ± 1, respectively, where Θ is the phase of $\phi_1(\omega)$. We hence focus on the behavior of $\int_0^\infty |\phi_1(\omega)| e^{-\alpha_1^i(\omega)x} d\omega$ in the limit of large x which can be estimated from a stationary phase approximation to be

$$\int_0^\infty |\phi_1(\omega)| e^{-\alpha_1^i(\omega)x} d\omega \sim |\phi_1(\omega_m)| \sqrt{\frac{2\pi}{x\dfrac{d^2\alpha_1^i}{d\omega^2}(\omega_m)}}\, e^{-\alpha_{1m}^i x} \tag{20}$$

As such, the selected wave mode is $\omega_m \sim 0.290\ \omega_0$ and its growth rate for both $|h_{max}-1|$ and $|h_{min}-1|$ is exponential with an exponent of $-\alpha_{1m}^i = 0.120$ (Figure 6). When $|h_{max}-1|$ and $|h_{min}-1|$ are tracked downstream in the numerical experiment of Figure 1, ω is found to be $0.291\ \omega_0$

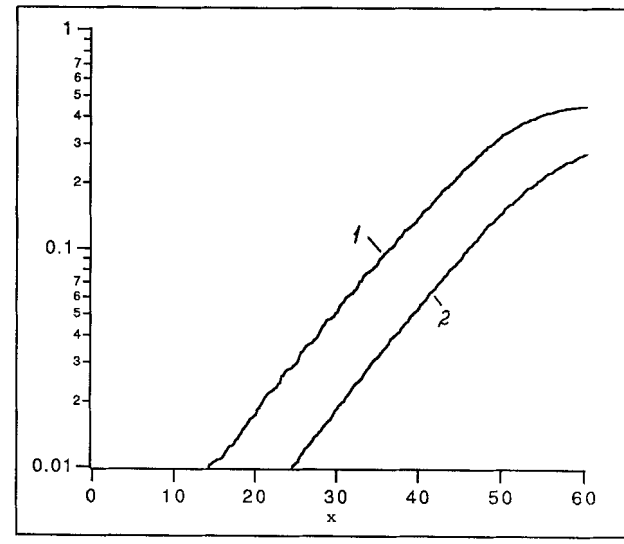

Figure 7. Spatial evolution of $|h_{max}-1|$ marked by line 1 and $|h_{min}-1|$ marked by line 2 downstream for Figure 1.

An exponential growth is evident.

with a spatial growth exponent of 0.108—very close to the linear theory and fully verifying the filtering mechanism that yields a nearly monochromatic wave within the inception region. The evolution of $|h_{max}-1|$ and $|h_{min}-1|$ is shown in Figure 7. These selected monochromated waves are quickly saturated, decelerated and compressed by the weakly nonlinear mechanism just beyond the inception region at $x = 50$.

The length of the inception region is quite sensitive to F_0. In Figure 8b, we show snapshots of the waves at various values of R for water with $F_0 = 5.0 \times 10^{-5}$. It is clear that, although the critical R is zero for the vertical film, an appreciable inception region is only apparent at R in excess of 1.5, the effective critical Reynolds number. It is also clear that from the snapshot in Figure 8b for $4R = 21$, corresponding to $\delta = 0.05$, pulses are not observed within the computation domain. Instead, small-amplitude KS chaos is observed. This is actually slightly beyond the transition δ value and after a long chaotic transient, regular pulses are still generated downstream beyond the computation domain shown in Figure 8. At lower δ values ($\delta < 0.03$), the KS chaos persists indefinitely downstream. For higher R values, distinct large-amplitude pulses are generated after the inception region as seen in Figure 8b. We use Stainthorp and Allen's criterion that the inception line is defined as when the wave amplitude first exceeds 10^{-4} cm to determine the beginning of the inception region for $F_0 = 10^{-4}$ and 10^{-5} for several values R for water. As seen in Figure 8a, the inception length drops rapidly from extremely high values around 1 m to about 10 cm for realistic values of R at both values of F_0 before it rises slowly again. It is also evident that Stainthorp and Allen's inception line can be accurately reproduced with $F_0 = 5 \times 10^{-5}$, which is the value we shall use to reproduce their downstream data.

With F_0 determined from the inception line, the dynamics is fully specified for Stainthorp and Allen's system if our random phase description of the noise is accurate. In Figure 9, our simulated wave speeds far beyond the inception region

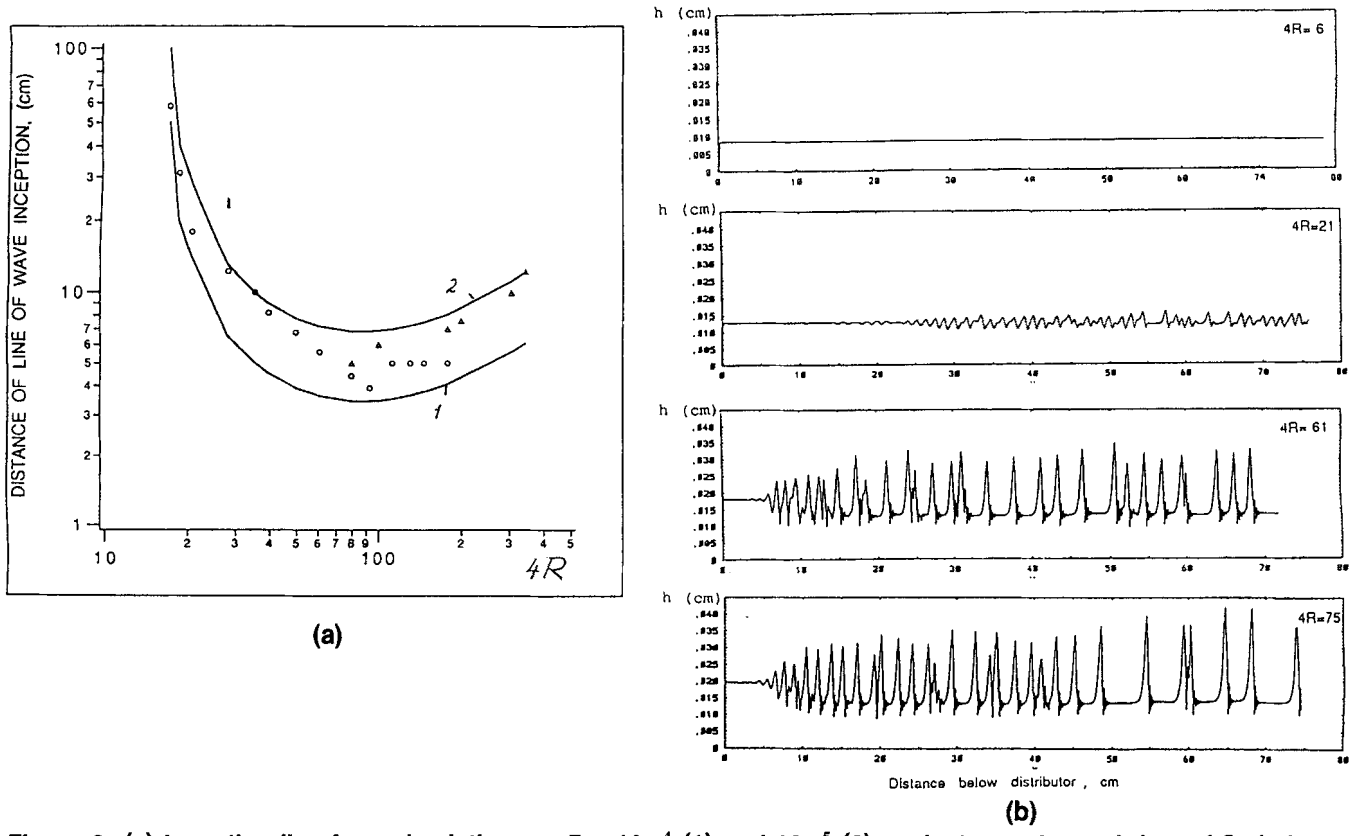

(a)

(b)

Figure 8. (a) Inception line from simulations at $F_0 = 10^{-4}$ (1) and 10^{-5} (2) against experimental data of Stainthorp and Allen (liquid is water); (b) the snapshots for the indicated R values at $F_0 = 0.5 \times 10^{-4}$.

are seen to be in quantitative agreement with their data for water at 3 values of R in a 30-cm-long channel. The deceleration from the linear phase speed 3 $\langle u \rangle$ by the weakly nonlinear mechanism followed by an acceleration after the pulses are formed is clearly evident. Stainthorp and Allen's channel is too short to reach the saturation region at 80 cm in Figure 2. More conclusive demonstration is shown in Figure 10, where their measured wave tracings for $4R = 75$ are compared directly to the simulated results. The average wave structure and spacing are faithfully reproduced. This fully verifies the accuracy of the BL equation and the ability to capture even some details of the wave dynamics and all the essential statistics with just two parameters—δ and F_0. It should be noted that the waves measured by Stainthorp and Allen in Figure 10 are inside a vertical tube, and they demonstrate appreciable transverse variation; yet, their dynamics and wave shapes are still captured by the two-dimensional simulation. This is consistent with our earlier observation that, until the transverse variation is so pronounced that it begins to pinch off adjacent crests to form "scallop waves," each cross section across the crest still behaves as a two-dimensional pulse with nearly two-dimensional wave dynamics (Chang et al., 1994).

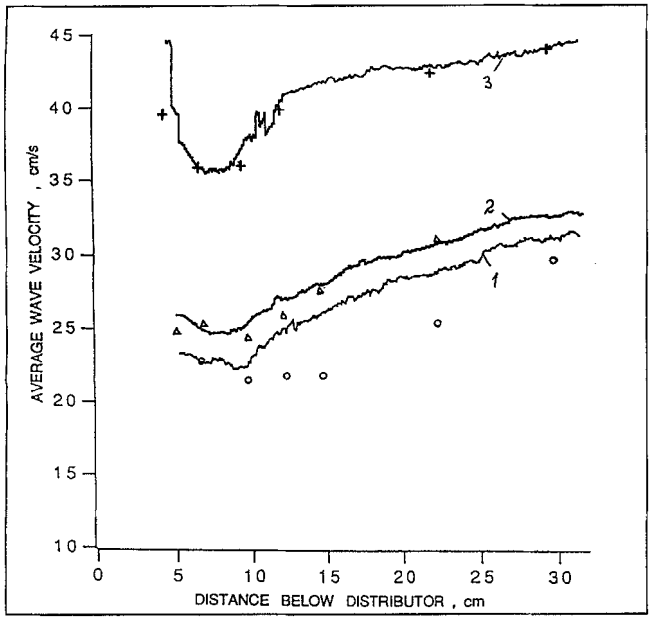

Figure 9. Simulated downstream evolution of time-averaged speed for (1) $4R = 60$, (2) $4R = 75$ and (3) $4R = 180$ with $F_0 = 5 \times 10^{-5}$ against Stainthorp and Allen's data for water represented by the symbols.

Statistical Analysis and Pulse Dynamics

From the above experiments, it is clear that pulses dominate most of the noise-driven wave dynamics on a long channel. In fact, the coarsening of its texture (pulse separation) and the accompanying increase in pulse speed downstream represent the most important wave dynamics specified by only δ and F_0. The pulse speed and separation no doubt plays an important role in heat-/mass-transfer enhancement, and an

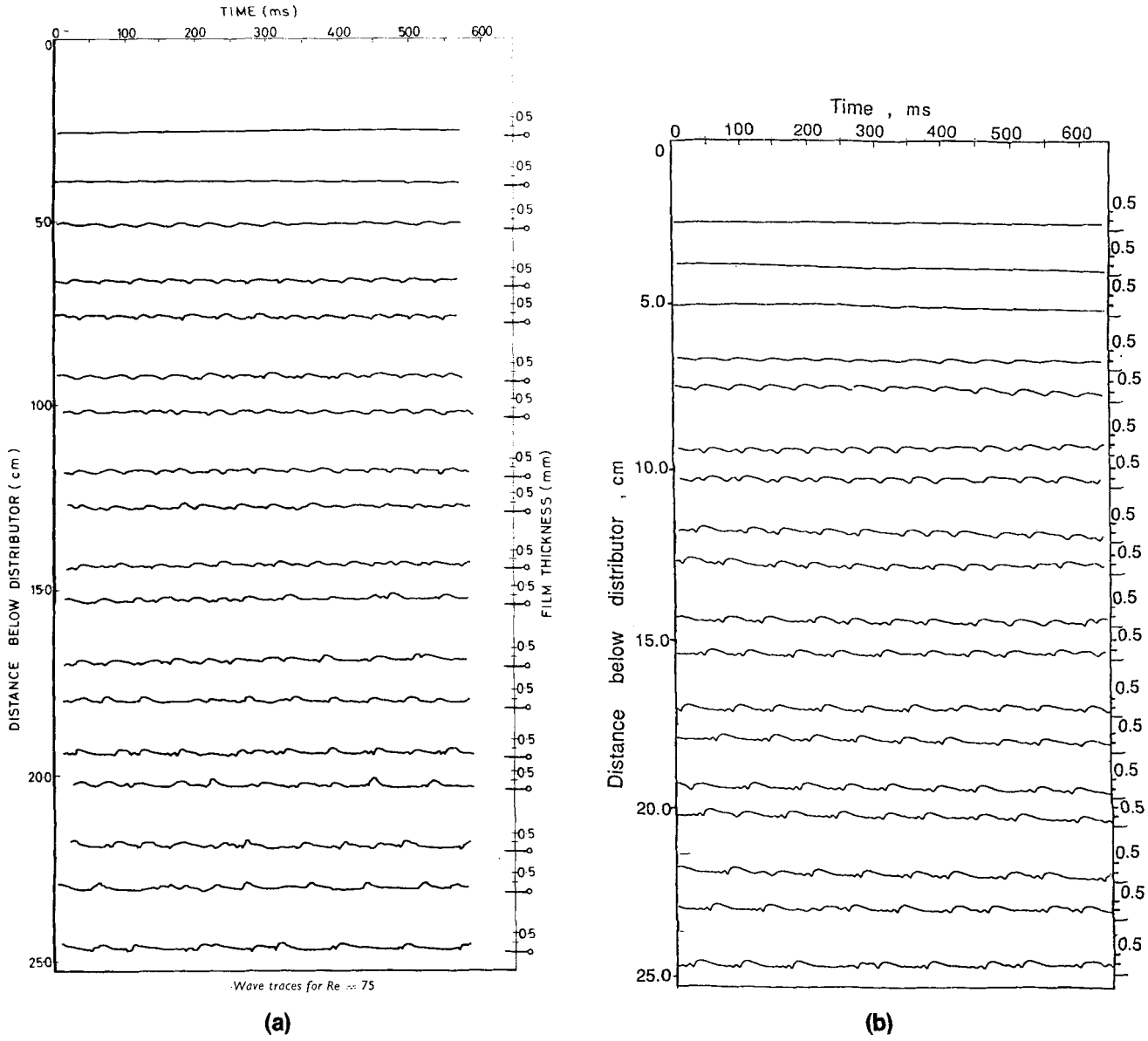

Figure 10. (a) Wave tracings of Stainthorp and Allen for $4R=75$; (b) simulated tracings with $F=5.0\times10^{-5}$ and $4R=75$ for water ($\gamma=2{,}850$).

understanding of their evolution downstream is an important preliminary to deciphering the enhancement mechanism. In our earlier work with the averaged equation (Chang et al., 1995a) and from Liu and Gollub's recent experiments, it is clear that the final stage coarsening and acceleration are due to the intermittent coalescence events whose frequency seems to be determined by F_0 although the individual pulses seem to have forgotten the small inlet noise. In both Liu and Gollub's experiment and our simulation, the wave slope remains small during the coalescence events and the BL equation still offers a good description. An intriguing modeling approach to this problem using a weakly interaction theory between pulses have been suggested in our earlier article (Chang et al., 1995a). However, an important premise of this approach is that the pulses are quasi-stationary at every spatial station. They surely evolve downstream as shown in Figure 2, but the stipulation is that such evolution is slow compared to the interaction time scale. This has been assumed in the past, and we scrutinize this assumption in detail with the accurate BL model equations.

In Figure 11, we depict the distributions of pulse speed and pulse spacing at various stations downstream. It is clear that while the downstream spacing beyond the monochromatic inception region is clearly widely distributed with a variance in excess of 50%, indicating again the pulses are not equally spaced even on the average, the speed distribution is very narrow with a 10% variance. The distribution of the pulse speed actually sharpens downstream beyond the inception region. This indicates that the pulses at every station travel at approximately the same speed, although they accelerate slowly from one station to another downstream.

This quasi-steady evolution can be visualized in the following manner. As the pulse density decreases downstream, the pulses must become larger and faster to carry the same flow

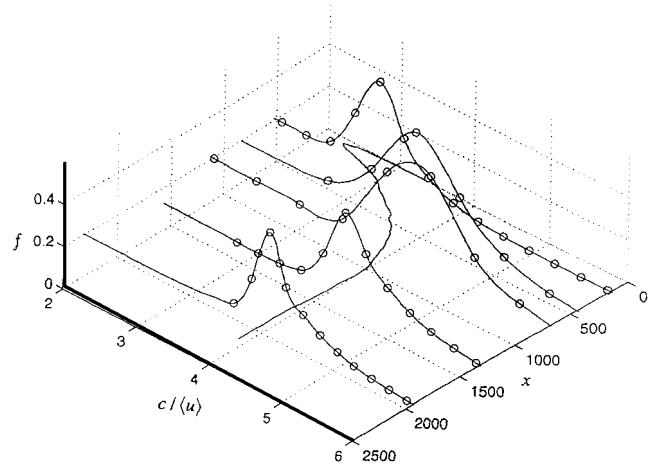

(a)

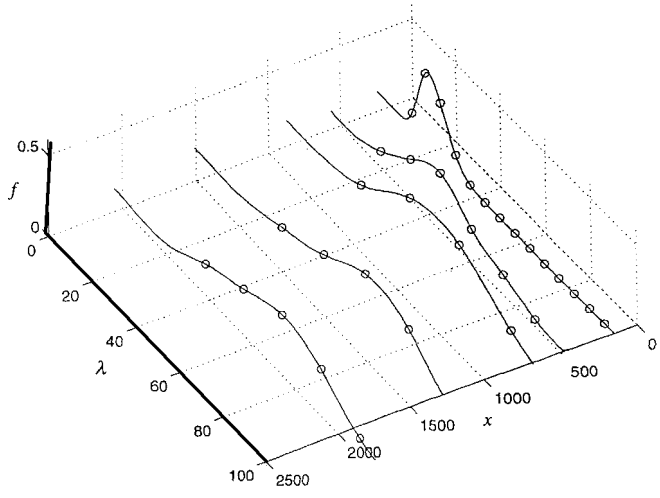

(b)

Figure 11. Pulse speed and spacing distributions at various spatial stations for conditions of Figure 1.

The downstream evolution of the mean velocity is also indicated. Both distributions begin beyond $x = 100$ units when the mean separation and speed are both increasing.

rate on the average. However, for a given δ the BL Eq. 1 only admits a single one-hump pulse traveling wave solution with $h(x \to \pm\infty) = 1$. The family of such pulse solutions is constructed for the simpler averaged equations earlier (Chang et al., 1993), and we have extended the result here to the BL equation seen in Table 1. The pulse area A in the table is defined as the portion above the substrate $A = \int_{-\infty}^{\infty}(h(x)-1)dx$. This implies that each larger and faster pulse actually lies on

Table 1. Solitary Pulse Data $[h(\pm\infty)=1]$

δ	c	A	h_{max}
0.02	3.451	1.043	1.191
0.04	5.194	4.390	1.925
0.06	7.145	11.871	2.880
0.08	7.407	16.482	3.145
0.10	7.458	20.587	3.272
0.12	7.710	27.054	3.509

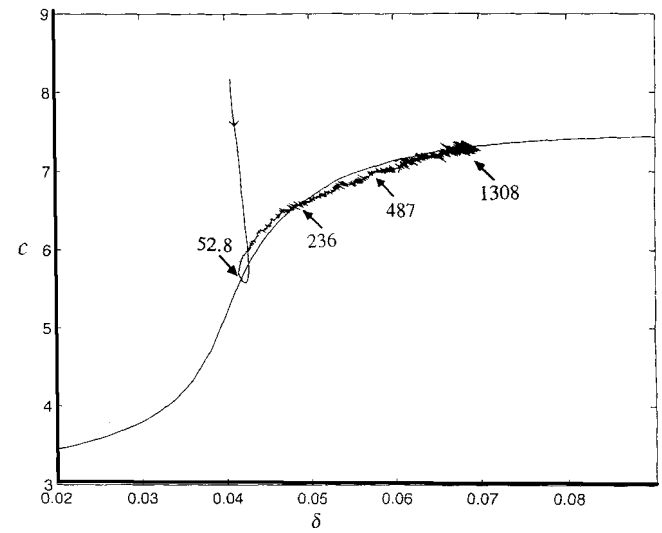

Figure 12. Evolution of Figure 1 lies along the pulse solution branch $c(\delta)$ after local normalization.

The downstream position in dimensionless x units is also indicated.

a thicker substrate and it corresponds to the pulse solution for that thickness s. This is verified by the slowly increasing substrate thickness in Figures 1 and 2. Conversely, if we normalize the local substrate thickness to unity at every spatial station, the local δ value will change downstream and each pulse at that location then corresponds to a pulse in the family of Table 1. We have found it easier to measure the average pulse area for this renormalization procedure than the thin substrate thickness by the following procedure. (See Chang et al., 1995a, for a more detailed demonstration for a different phenomenon.) Since the stationary version of Eq. 1 in the moving frame is invariant to $x \to s^{1/3}x$, $h \to sh$, $q \to s^3q$, $c \to s^2c$, $A \to s^{4/3}A$ and $\delta \to s^{11/3}\delta$, where A is the area above the substrate and s the substrate thickness, the local δ value corresponding to $s = 1$ is simply given by

$$(\delta/\delta_0) = [A(\delta)/A(\delta_0)]^{11/4} \tag{21}$$

where δ_0 is the reference value corresponding to the Nusselt flat film with the inlet flow rate and the area A is tabulated in Table 1. A similar scaling can also be constructed to obtain the local pulse speed

$$[c(\delta)/c(\delta_0)] = [A(\delta)/A(\delta_0)]^{3/2} \tag{22}$$

We note that this renormalization corresponds to a rescaling of the local pulse speed c to the local $\langle u \rangle$ in the substrate. The downstream evolution of the local c and δ from our simulation is plotted in Figure 12 against the pulse solution branch $c(\delta)$ for pulse traveling waves in Table 1 with $h(x \to \pm\infty) = 1$. It is clear that the evolution trajectory follows the pulse solution branch very closely beyond the inception region. This indicates that the pulses are, on the average, very close to a quasi-stationary traveling pulse at every station.

That the pulses are traveling wave solutions also suggests an intriguing artifact. Periodically separated pulses represent

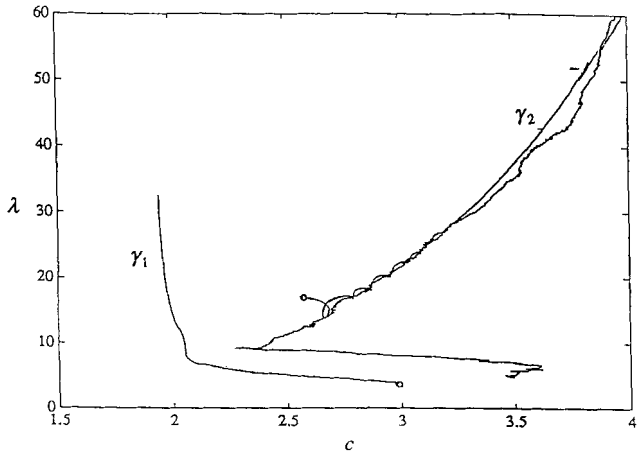

Figure 13. Evolution along the γ_2 periodic solution branch showing roughly linear correlation between time-average spacing and speed downstream.

periodic wave solutions with large wavelengths. However, due to mass conservation considerations and because the pulse speed is so narrowly distributed at every station, the average spacing at every station is close to a periodic pulse train with the same flow rate. However, since the average separation λ increases downstream while the average flow rate at every station must be the same, the average pulse speed c must increase roughly linearly with respect to the separation since most of the liquid is carried by the pulses. (See Nakaya, 1989, for a more mathematical discussion of this simple mass conservation argument.) This increase in average speed is the same for either a periodic train of pulses or identical pulses with irregular spacing. As a result, the downstream evolution of the unnormalized pulse speed and pulse separation should follow the periodic solution branch for the given δ of the flat-film solution (0.216 in Figure 1). This is clearly true when the simulated result is overlaid in Figure 13 on the 1-hump periodic solution branch γ_2 (see Chang et al., 1993, for a discussion of the periodic solution branches based on the simpler averaged equations). However, the pulses are clearly not periodically spaced. It is precisely because they are all close to a pulse traveling wave that their time-averaged behavior follows that of a periodic train of pulses due to simple mass conservation considerations. This is an almost trivial example of how "hidden symmetries" can render the time-averaged picture of a sequence of spatially and temporally chaotic images very regular (Gluckman et al., 1993). In this case, the hidden symmetries are simply the quasi-steady propagating manners of the pulses and simple mass conservation.

We note that the evolution just beyond the inception region also follows the small-amplitude waves of the γ_1 periodic solution branch quite closely. This is not as surprising since waves in that region are very close to being periodic and, in fact, monochromatic as seen in Figures 1, 3, 4, 5 and 8. The minimum in wave speed c is reached when the wavelength of the monochromatic wave comes close to the wavelength $\lambda = 8.2$ predicted by our earlier weakly nonlinear theory (Chang et al., 1993). This is slightly below the wavelength $\lambda = 11$ of the linearly fastest growing mode at inception.

The remaining modeling tasks for wave dynamics are to determine the coalescence frequency and its dependence on δ and F_0 to capture the evolution speed along the trajectories in Figures 12 and 13 that is driven by the coalescence. This is an ongoing effort in our group, and a statistical model will soon offer explicit and generic correlations for the roughly linear increase in spacing and speed in Figure 2 and the final saturated values. This theory will rely on the observation here that noise-driven dynamics can be simulated with a random-phase description of the inlet noise. In essence, such inlet noise determines the density of large pulses which precipitate coalescence. The "pair-distribution" function of these large pulses, which specifies the probability that two consecutive pulses are large and offers an estimate of the variance of the spacing distribution in Figure 10b, is also specified by noise. However, how these large pulses catch up with the smaller ones and whether the resulting interaction ends in a coalescence event is essentially the deterministic intrinsic dynamics we have already modeled with our binary interaction theory (Chang et al., 1995a). Consequently, in contrast to the speculation of Huerre and Monkewitz, the roles of noise-driven and intrinsic dynamics can be easily discerned for this convectively unstable system. This is because, at a sufficiently high flow rate, the downstream dynamics is dominated by very coherent spatially localized pulses which are themselves convectively stable and whose only dependence on noise is on its amplitude and separation. Moreover, such dependence can be precisely modeled with a mean field statistical theory since random-phase noise can accurately reproduce observed wave dynamics. Because of such unique features, dynamics on a freely falling film may be the first convectively unstable open-flow system whose spatio-temporal patterns and their dependence on noise can be fully understood.

Acknowledgment

This work has been supported by a grant from DOE.

Notation

F = zero-mean flow rate forcing at the inlet
g = gravitational acceleration
h = film height scaled with respect to h_0
h_{max} = pulse amplitude
H = channel height of a closed distributor scaled with respect to h_0
L = channel length scaled by $h_0\kappa$
M = number of frequency unit
N = number of basis
$\langle q \rangle$ = flow rate of Nusselt flat film per span width
R = Reynolds number based on average flow rate per span width $\langle q \rangle = \langle u \rangle h_0$ of the flat film
t = dimensionless time scaled with respect to $h_0\kappa/\langle u \rangle$
$\langle u \rangle$ = cross-film average tangential velocity of the flat film
v = normal velocity scaled by $\langle u \rangle/\kappa$
x = tangential coordinate scaled by $h_0\kappa$
y = normal coordinate scaled by h_0

Greek letters

α = complex wave number
δ = normalized Reynolds number defined in Eq. 2, based either on the Nusselt flat film or the average local substrate thickness s
η = normal coordinate of transformed domain
λ = wavelength, pulse spacing, dimensional
ν = kinematic viscosity

ρ = density
σ = interfacial tension
σ = zero-frequency spatial eigenvalue
$\phi_k(\omega)$ = Fourier coefficients of the film height
φ = disturbance to u
$\psi_k, \bar{\psi}_k$ = basis functions in η direction
ω_0 = neutral frequency

Literature Cited

Alekseenko, S. V., V. E. Nakoryakov, and B. G. Pokusaev, "Wave Formation on a Vertically Falling Film," *AIChE J.*, **31,** 1446 (1985).

Benjamin, T. B., "Wave Formation in Laminar Flow Down an Inclined Plane," *J. Fluid Mech.*, **2,** 554 (1957).

Benney, B. J., "Long Waves in Liquid Films," *J. Math. Phys.*, **45,** 150 (1966).

Chang, H.-C., "Evolution of Nonlinear Waves on Vertically Falling Films—A Normal Form Analysis," *Chem. Eng. Sci.*, **42,** 515 (1987).

Chang, H.-C., "Onset of Nonlinear Waves on Falling Films," *Phys. Fluids*, **A1,** 1314 (1989).

Chang, H.-C., E. A. Demekhin, and D. I. Kopelevich, "Nonlinear Evolution of Waves on a Vertically Falling Film," *J. Fluid Mech.*, **250,** 443 (1993).

Chang, H.-C., "Wave Evolution on a Falling Film," *Ann. Rev. of Fluid Mech.*, **26,** 103 (1994).

Chang, H.-C., M. Cheng, E. A. Demekhin, and D. I. Kopelevich, "Secondary and Tertiary Excitation of Three-Dimensional Patterns on a Falling Film," *J. Fluid Mech.*, **270,** 251 (1994).

Chang, H.-C., E. A. Demekhin, and E. Kalaidin, "Interaction Dynamics of Solitary Waves on a Falling Film," *J. Fluid Mech.*, **294,** 123 (1995a).

Chang, H.-C., E. A. Demekhin, and D. I. Kopelevich, "Stability of Solitary Pulses to Wavepacket Disturbances in an Active Medium," *Phys. Rev. Lett.*, **75,** 1747 (1995b).

Cheng, M., and H.-C. Chang, "Stability of Axisymmetric Waves on Liquid Films Flowing Down a Vertical Column to Azimuthal and Streamwise Disturbances," *Chem. Eng. Commun.*, **118,** 327 (1992).

Cheng, M., and H.-C. Chang, "Competition between Sideband and Subharmonic Secondary Instability on a Falling Film," *Phys. Fluid*, **6,** 34 (1995).

Demekhin, E. A., and V. Ya. Shkadov, "Two-Dimensional Wave Regimes of a Thin Liquid Film," *Izv. Akad. Nauk SSSR, Mekh. Zhidk. Gaza.*, **3,** 63 (1985).

Demekhin, E. A., M. A. Kaplan, and V. Ya. Shkadov, "Mathematical Models of the Theory of Viscous Liquid Films," *Izv. Akad. Nauk SSSR, Mekh. Zhidk. Gaza.*, **6,** 73 (1987).

Dukler, A. E., "The Wavy Gas-Liquid Interface," *Chem. Eng. Educ.*, 108 (1976).

Fasel, H. F., U. Rist, and U. Konzelmann, "Numerical Investigation of the Three-Dimensional Development in Boundary Layer Transition," *AIAA*, **87,** 1203 (1987).

Frisk, D. P., and E. J. Davis, "The Enhancement of Heat Transfer by Waves in Stratified Gas-Liquid Flow," *Int. J. Heat Mass Transf.*, **15,** 1537 (1972).

Gluckman, B. J., P. Marcq, J. Bridger, and J. P. Gollub, "Time-Averaging of Chaotic Spatiotemporal Wave Patterns," *Phys. Rev. Lett.*, **71,** 2034 (1993).

Henstock, W. H., and T. J. Hanratty, "Gas Absorption by a Liquid Layer Flowing on the Wall of a Pipe," *AIChE J.*, **25,** 122 (1979).

Ho, L. W., and A. T. Patera, "A Legendre Spectral Element Method for Simulation of Unsteady Incompressible Viscous Surface Flow," *Comp. Methods Appl. Mech. Eng.*, **80,** 355 (1990).

Huerre, P., and P. A. Monkewitz, "Local and Global Instabilities in Spatially Developing Flows," *Ann. Rev. of Fluid Mech.*, **22,** 473 (1990).

Joo, S. W., S. H. Davis, and S. G. Bankoff, "On Falling Film Instabilities and Wave Breaking," *Phys. Fluids*, **A3,** 231 (1991).

Joo, S. W., and S. H. Davis, "Instabilities of Three-Dimensional Viscous Falling Films," *J. Fluid Mech.*, **242,** 529 (1992).

Kapitza, P. L., "Wave Flow of a Thin Viscous Fluid Layers," *Zh. Eksp. Teor. Fiz.*, **18,** 1 (1948).

Khesghi, H. A., and L. E. Scriven, "Disturbed Film Flow on a Vertical Plane," *Phys. Fluids*, **35,** 990 (1987).

Krantz, W. B., and S. L. Goren, "Stability of Thin Liquid Films Flowing Down a Plane," *Ind. Eng. Chem.*, **10,** 91 (1971).

Levich, V. G., *Physiochemical Hydrodynamics*, Prentice-Hall, Englewood Cliffs, NJ (1962).

Li, Y. T., and I. C. Ho, "A New Evaporator Tube Design," *Desalination*, **65,** 87 (1987).

Lin, S. P., "Finite Amplitude Stability of a Parallel Flow with a Free Surface," *J. Fluid Mech.*, **36,** 113 (1969).

Lin, S. P., *Film Waves in Waves on Fluid Interfaces*, R. E. Meyer, ed., Academic Press, p. 261 (1983).

Liu, J., J. P. Paul, and J. P. Gollub, "Measurement of the Primary Instabilities of Film Flows," *J. Fluid Mech.*, **220,** 69 (1993).

Liu, J., and J. P. Gollub, "Solitary Wave Dynamics on Film Flows," *Phys. Fluid*, bf 6, 1702 (1994).

Malamataris, N. T., and T. C. Papanastasiou, "Unsteady Free Surface Flows on Truncated Domains," *Ind. Eng. Chem. Res.*, **30,** 2210 (1991).

Nakaya, C., "Waves on a Viscous Fluid Film Down a Vertical Wall," *Phys. Fluids*, **A1,** 1143 (1989).

Pierson, F. W., and S. Whitaker, "Some Theoretical and Experimental Observation of Wave Structure of Falling Films," *Ind. Eng. Chem. Fund.*, **16,** 401 (1977).

Portalski, S., and A. J. Clegg, "An Experimental Study of Falling Liquid Films," *Chem. Eng. Sci.*, **27,** 1257 (1972).

Pumir, A., P. Manneville, and Y. Pomeau, "On Solitary Waves Running Down an Inclined Plane," **135,** 27 (1983).

Roberts, A. J., "Boundary Conditions for Approximate Differential Equations," *J. Austral. Math. Soc.*, **B34,** 54 (1992).

Salamon, T. R., R. C. Armstrong and R. A. Brown, "Travelling Waves on Inclined Films: Numerical Analysis by the Finite-Element Method," *Phys. Fluid*, **6,** 2202 (1994).

Shkadov, V. Ya., "Wave Conditions in the Flow of Thin Layer of a Viscous Liquid Under the Action of Gravity," *Izv. Akad. Nauk. SSSR Mekh. Zhidk i Gaza*, **1,** 43 (1967).

Stainthorp, F. P., and J. M. Allen, "The Development of Ripples on the Surface of Liquid Film Flowing Inside a Vertical Tube," *Trans. Inst. Chem. Eng.*, **43,** 85 (1965).

Tsvelodub, O. Yu., "Steady Travelling Waves on a Vertical Film of Fluid," *Izv. Akad. Nauk SSSR, Mekh. Zhidk. i Gaza.*, **4,** 142 (1980).

Wasden, F. K., and A. E. Dukler, "Insights into the Hydrodynamics of Free Falling Wavy Films," *AIChE J.*, **35,** 187 (1989).

Yih, C.-S., "Stability of Liquid Flowing Down an Inclined Plane," *Phys. Fluids*, **6,** 34 (1963).

Manuscript received June 16, 1995, and revision received Sept. 11, 1995.